Electronic Supplementary Material (ESI) for Physical Chemistry Chemical Physics.

Supplementary Information for: ELDOR-detected NMR beyond hyperfine couplings: A case study with Cu(II)-porphyrin dimers

Nino Wili,[a] Sabine Richert,[b,‡] Bart Limburg,[c] Simon J. Clarke,[d] Harry L. Anderson,[c] Christiane R. Timmel,[b] and Gunnar Jeschke[a]

[a] *Laboratorium für Physikalische Chemie, ETH Zürich, Vladimir-Prelog-Weg 2, 8093 Zürich, Switzerland. E-mail: gjeschke@ethz.ch* [b] *Centre for Advanced Electron Spin Resonance (CÆSR), University of Oxford, South Parks Road, Oxford, OX1 3QR, UK.* [c] *Chemistry Research Laboratory, University of Oxford, Mansfield Road, Oxford, OX1 3TA, UK.* [d] *Inorganic Chemistry Laboratory, University of Oxford, South Parks Road, Oxford, OX1 3QR, UK.*

‡ *Present address: Institut für Physikalische Chemie, Albert-Ludwigs-Universität Freiburg, Albertstr. 21, 79104 Freiburg, Germany.*

Contents

S.1 Synthesis and characterisation of CuP2 and *f*-CuP2

S.1.1 General

The reagents were purchased from commercial sources. The solvents were used as supplied (analytical / HPLC-grade from Fisher or Sigma-Aldrich) or, if dry solvents were required, taken from a solvent drying system (MBraun MB-SPS-5-Bench Top) under nitrogen atmosphere (H_2O content <20 ppm as determined by Karl Fischer titration). Petrol ether (PE) over a boiling point range of 40-60°C was used. Eluent mixtures are reported in volume:volume. Column chromatography was carried out using Merck Geduran silica gel 60 under N_2 pressure. TLC was carried out on Merck silica gel 60 F254 Al plates. MALDI-TOF-MS was carried out in positive reflectron mode using a Waters MALDI-micro X instrument. NMR spectra were recorded using a Bruker AVII400 or AVII500 instrument. All peaks were referenced to the residual solvent peak. UV-vis spectra were recorded using a PerkinElmer Lambda 25 instrument. Size exclusion chromatography (SEC) was carried out using Bio-Beads S-X1, 200-400 mesh (Bio Rad). Analytical gel permeation chromatography (GPC) was performed on a JAIGEL H-P pre-column, a JAIGEL 3H-A (8 mm x 500 mm) and a JAIGEL 4H-A column (8 mm x 500 mm) in series with tetrahydrofuran/1% pyridine as eluent. The structures of the compounds used in this study, including precursors, are shown in Fig. S1. Porphyrin precursors **H_2P_H** and **ZnP_H** were synthesized according to a literature procedure.[1] Porphyrin dimers **$ZnP2_H$** and **f-$ZnP2_{Br}$** were synthesized according to a literature procedure.[2]

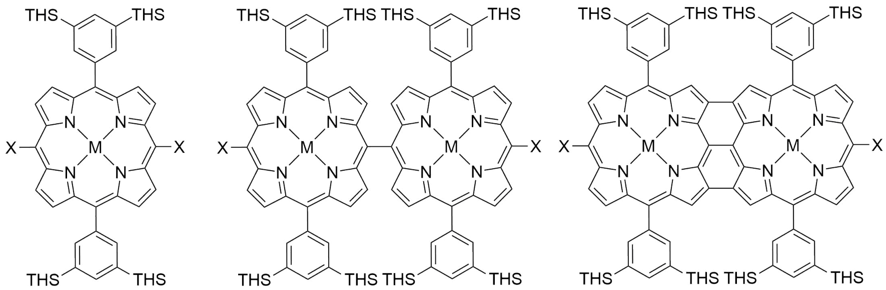

M = Zn, X = H, **ZnP_H**
M = 2H, X = H, **H_2P_H**
M = Cu, X = H, **CuP_H**

M = Zn, X = H, **$ZnP2_H$**
M = Zn, X = Br, **$ZnP2_{Br}$**
M = Cu, X = H, **$CuP2_H$**

M = Zn, X = H, **f-$ZnP2_H$**
M = Zn, X = Br, **f-$ZnP2_{Br}$**
M = Cu, X = H, **f-$CuP2_H$**

Fig. S1 Chemical structures of the porphyrin compounds used in this study. Note that throughout the main article, **$CuP2_H$** is denoted as **CuP2**, and **f-$CuP2_H$** is denoted as ***f*-CuP2**.

S.1.2 Synthesis of f-$CuP2_H$

f-$ZnP2_H$ (2.97 mg, 0.9 μmol) was dissolved in DCM (0.5 mL) and a solution of TFA (50 μL in 0.5 mL DCM) was added. The solution was stirred for 5 minutes after which it was quenched by addition of saturated aqueous $NaHCO_3$ (1 mL). The solution was stirred vigorously for 5 minutes after which the aqueous layer was removed. Next, $Cu(OAc)_2$ (9 mg, 45 μmol) and MeOH (0.1 mL) were added and the mixture heated to 45°C for 2 hours. The product was isolated by chromatography (SiO_2, PE/DCM 1/1) in 74% yield (2.21 mg). m/z (MALDI-TOF, DCTB): 3302.11 ($[M]^+$ calcd. 3302.82). UV-vis / NIR ($CHCl_3$) λ_{max} / nm (ε / $mM^{-1}cm^{-1}$): 404 (131), 552 (85.1), 572 (83.1), 665 (9.24), 984 (17.1). The GPC trace shows a single peak, see Fig. S2.

S.1.3 Synthesis of $CuP2_H$

$ZnP2_H$ (12.96 mg, 3.9 μmol) was dissolved in DCM (0.5 mL) and a solution of TFA (50 μL in 0.5 mL DCM) was added. The solution was stirred for 5 minutes after which it was quenched by addition of saturated aqueous $NaHCO_3$ (1 mL). The solution was stirred vigorously for 5 minutes after which the aqueous layer was removed. Next, $Cu(OAc)_2$ (39 mg, 0.2 mmol) and MeOH (0.1 mL) were added and the mixture heated to 45°C for 2 hours. The product was isolated by chromatography (SiO_2, PE/DCM

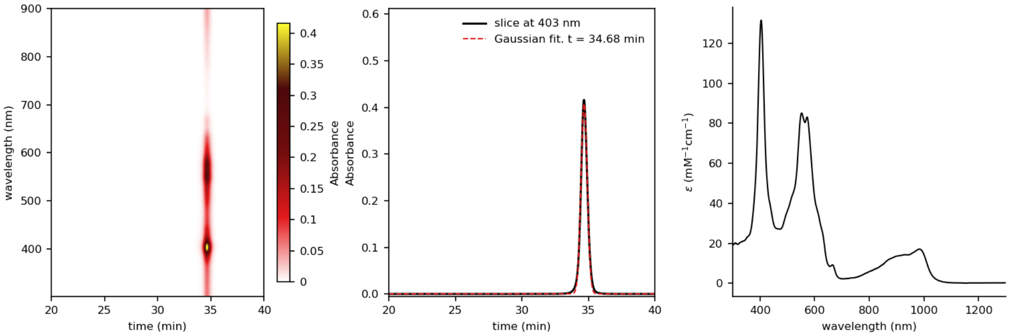

Fig. S2 Left: Gel permeation chromatography of ***f*-CuP2**$_{\mathbf{H}}$. Conditions: THF / 1% pyridine, 1 mL min^{-1}, JAIGEL H-P pre-column, a JAIGEL 3H-A (8 mm x 500 mm) and a JAIGEL 4H-A column (8 mm x 500 mm) in series, room temperature. Middle: time-GPC trace at 403 nm and corresponding Gaussian fit. Right: UV-vis / NIR spectrum of ***f*-CuP2**$_{\mathbf{H}}$ in $CHCl_3$.

5/1) in 69% yield (8.7 mg). m/z (MALDI-TOF, dithranol): 3306.65 ($[M]^+$ calcd. 3306.85). UV-vis / NIR ($CHCl_3$) λ_{max} / nm (ε / $mM^{-1}cm^{-1}$): 411 (122), 441 (95.2), 544 (26.4), 581 (5.32). The GPC trace shows a single peak, see Fig. S3.

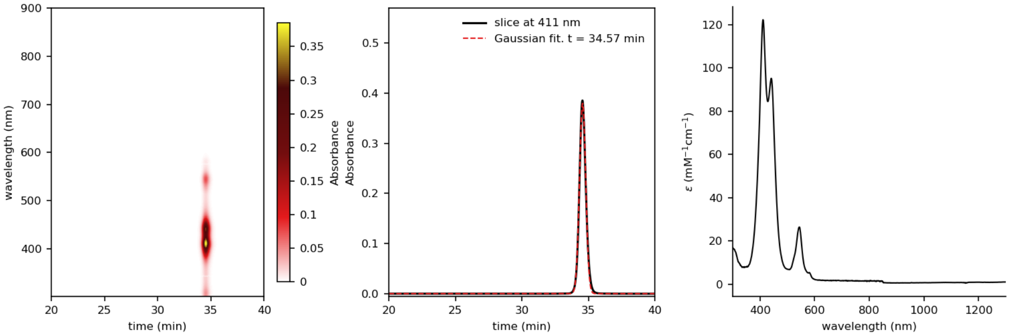

Fig. S3 Left: Gel permeation chromatography of **CuP2**$_{\mathbf{H}}$. Conditions: THF / 1% pyridine, 1 mL min^{-1}, JAIGEL H-P pre-column, a JAIGEL 3H-A (8 mm x 500 mm) and a JAIGEL 4H-A column (8 mm x 500 mm) in series, room temperature. Middle: time-GPC trace at 411 nm and corresponding Gaussian fit. Right: UV-vis / NIR spectrum of **CuP2**$_{\mathbf{H}}$ in $CHCl_3$.

S.1.4 Synthesis of *f*-ZnP2$_{\mathbf{H}}$

***f*-ZnP2**$_{\mathbf{Br}}$ (10.34 mg, 2.98 μmol) was dissolved in dry THF (5 mL) and $NaBH_4$ (0.55 mg, 14.9 μmol) and $[Pd(PPh_3)_4]$ (0.34 mg, 0.29 μmol) were added. The mixture was deaerated by Ar-purging and subsequently heated to 65°C for 1.5 h. H_2O (5 mL) was added and the mixture extracted with DCM. The organic layer was evaporated and the crude material was purified by column chromatography (SiO_2, 95:5 PE/DCM) to yield ***f*-ZnP2**$_{\mathbf{H}}$ (8.50 mg, 2.57 μmol, 86%). m/z (MALDI-TOF, dithranol): 3305.54 ($[M]^+$ calcd. 3306.49). ^{1}H NMR (400 MHz, $CDCl_3$) δ 8.38 (s, 2H), 8.06 (d, J = 4.5 Hz, 4H), 7.85 (s, 8H), 7.82 (s, 4H), 7.57 (d, J = 4.5 Hz, 4H), 7.24 (s, 4H), 1.49 - 1.15 (m, 192H), 0.92 - 0.75 (m, 120H). See Fig. S4. UV-vis / NIR ($CHCl_3$) λ_{max} / nm (ε / $mM^{-1}cm^{-1}$): 412 (87.3), 455 (28.3), 557 (63.2), 942 (7.90), 1066 (11.1). The GPC trace shows a single peak, see Fig. S5.

S.1.5 Synthesis of CuP$_{\mathbf{H}}$

To a solution of free base porphyrin **H$_2$P$_{\mathbf{H}}$** (18.0 mg, 11.3 μmol) in DCM (1 mL) was added $Cu(OAc)_2$ (113 mg, 56.0 μmol) in MeOH (0.1 mL) and the mixture heated to 45°C for 2 hours. The mixture was evaporated and the product was isolated by column chromatography (SiO_2, PE/DCM 5/1) in 81%

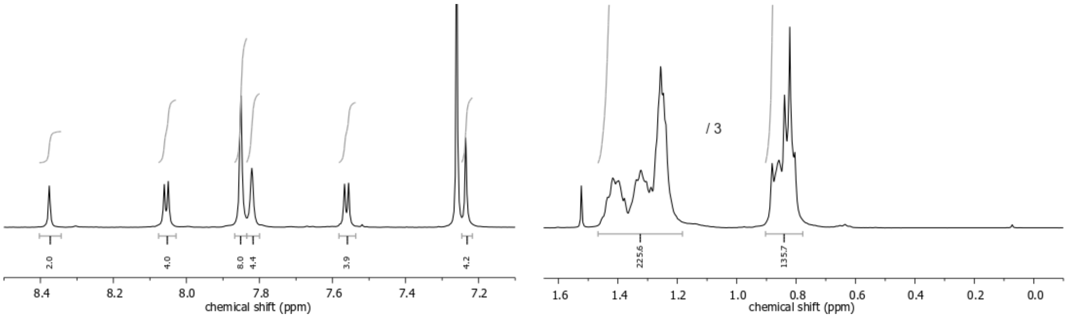

Fig. S4 ^{1}H NMR spectrum of ***f*-ZnP2**$_{\mathbf{H}}$ in CDCl$_3$ (400 MHz).

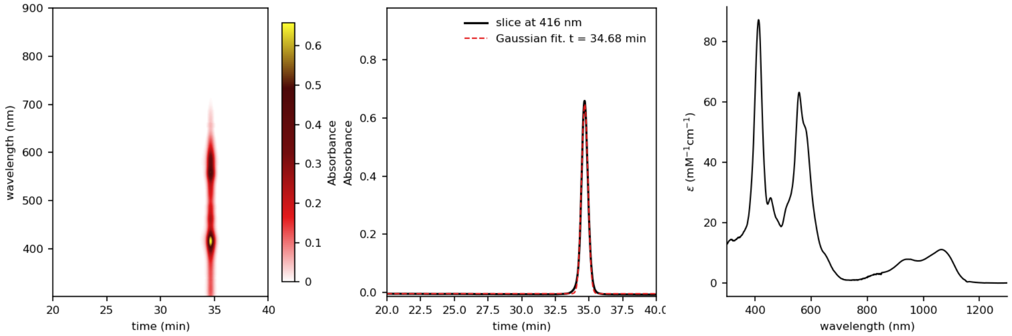

Fig. S5 Left: Gel permeation chromatography of ***f*-ZnP2**$_{\mathbf{H}}$. Conditions: THF / 1% pyridine, 1 mL min^{-1}, JAIGEL H-P pre-column, a JAIGEL 3H-A (8 mm x 500 mm) and a JAIGEL 4H-A column (8 mm x 500 mm) in series, room temperature. Middle: time-GPC trace at 416 nm and corresponding Gaussian fit. Right: UV-vis / NIR spectrum of ***f*-ZnP2**$_{\mathbf{H}}$ in CHCl$_3$.

yield (15.2 mg). m/z (MALDI-TOF, DCTB): 1654.4 ([M]$^+$ calcd. 1654.4). UV-vis / NIR (CHCl$_3$) λ_{max} / nm (ε / mM^{-1}cm^{-1}): 408 (348), 530 (16.4), 563 (2.9). The GPC trace shows a single peak, see Fig. S6.

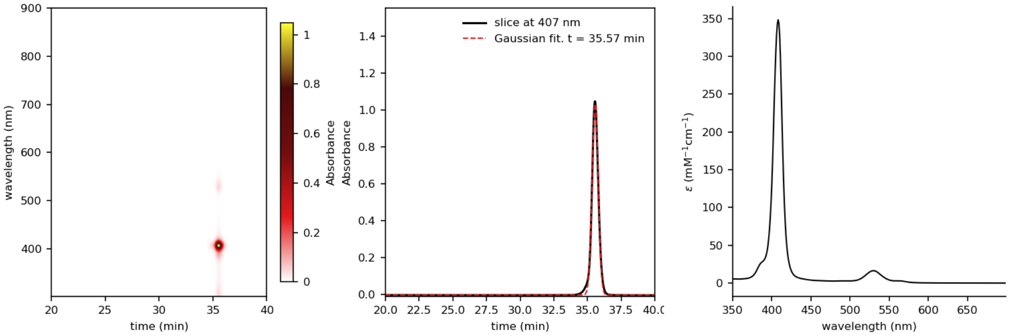

Fig. S6 Left: Gel permeation chromatography of **$\mathbf{CuP_H}$**. Conditions: THF / 1% pyridine, 1 mL min^{-1}, JAIGEL H-P pre-column, a JAIGEL 3H-A (8 mm x 500 mm) and a JAIGEL 4H-A column (8 mm x 500 mm) in series, room temperature. Middle: time-GPC trace at 407 nm and corresponding Gaussian fit. Right: UV-vis / NIR spectrum of **$\mathbf{CuP_H}$** in $CHCl_3$.

S.2 EPR setup

All pulsed Q-band EPR measurements except for ENDOR were performed on a home-built Q-band spectrometer based on a Keysight M8190A Arbitrary Waveform Generator (AWG).[3] Transients were recorded with a SP Devices ADQ421 ADC with a sampling frequency of 2 GHz. The pulses were amplified by a traveling wave tube (TWT) amplifier with 150 W nominal output power. Broadband Q-band resonators that can accommodate 3 mm tubes were used. We would like to emphasize that neither the AWG nor the high output power is necessary to perform the EDNMR measurements discussed in this paper. This particular spectrometer was used here for convenience due to its highly flexible software for experiment setup. It is crucial, however, that the resonator has a large bandwidth in order to access the large nuclear frequencies.

The hole burning pulses were generally of Gaussian type with the functional form

$$f(t) = \nu_1 \cdot \exp\left(-\frac{4\ln(2)}{(0.4t_p)^2} \cdot (t - t_p/2)^2\right), \tag{1}$$

where t_p is the pulse length given below. Note that the simulations did assume rectangular pulses. For the simulation input, we therefore scaled the experimentally estimated ν_1 by a factor of 0.42, which corresponds to the ratio of integrals of the Gaussian pulse and a rectangular pulse. Note that the EDNMR spectra presented here are not *very* sensitive to the *exact* pulse settings.

Davies ENDOR measurements were carried out at Q-band frequencies on a Bruker ELEXSYS E580 pulsed EPR spectrometer equipped with a Bruker EN 5107D2 resonator and an Oxford Instruments liquid helium flow cryostat (CF935).

CW EPR spectra were recorded at 20 K at X-band frequencies (9.5 GHz) using a Bruker ELEXSYS E500 spectrometer including a Bruker super high Q resonator.

Additional details about the exact experimental parameters for each figure are given at the end of the ESI.

S.3 Characterization of the resonator

The resonator profile was characterized by transient nutation measurements with the sequence t_p - T - Hahn echo, where t_p was typically swept from 0 to 64 ns in 1 ns steps.[4] The experiment was then carried out at different frequencies ν_{mw}. For each frequency, the magnetic field was adjusted such that the maximum of the EDFS spectrum was observed. The process is fully automated in our spectrometer and typically takes around 5 minutes. A damped oscillation was fitted to each nutation trace to extract the nutation frequency ν_1. A resonator profile of the form

$$\nu_1(\nu_{\mathrm{mw}}) = \nu_{1,\mathrm{max}} \cdot \left[1 + \left(2 \cdot Q \cdot \frac{(\nu_{\mathrm{mw}} - \nu_0)}{\nu_0}\right)^2\right]^{-1/2} \tag{2}$$

was then fitted to the experimental data points of $\nu_1(\nu_{\mathrm{mw}})$.

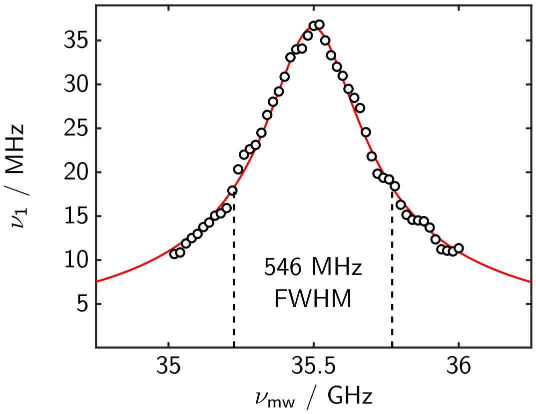

Fig. S7 Typical magnitude frequency response of the resonator as used for the EDNMR measurements.

A typical resonator profile is shown in Fig. S7. Our resonator usually showed Q-values around 110, which corresponds to a full width at half maximum (FWHM) of over 500 MHz, allowing experiments in the ultra wide-band (UWB) range. Another common definition of the bandwidth uses the -3 dB points, which gives around 320 MHz in our case.

Note that the nutation curves of ***f*-CuP2** are not well-defined, see below. The strong level mixing leads to a broad distribution of transition moments even in the absence of microwave inhomogeneity. The effective nutation frequency was found to be field dependent (data not shown). Since the resonator mode could be very well reproduced between several measurements with **CuP2**, we used the same Q-factor for all simulations.

S.4 SQUID setup

Samples of $\mathbf{CuP_H}$ (8.81 mg) or $\boldsymbol{f}$**-**$\mathbf{CuP2_H}$ (4.43 mg) were transferred with the aid of PE into NMR tubes. PE was used to wash down the sample to create a film only around the bottom of the tube, and the solvent was evaporated. The tube was flame-sealed under vacuum to a length of 6 cm and introduced at the correct height into the SQUID with the aid of a plastic straw.

DC measurements were performed using a Quantum Design MPMS-XL SQUID magnetometer. The magnetic moment of the sample was measured in the temperature range 2−300 K, using 0.1 K steps below 10 K, 2 K steps from 10−100 K and 5 K steps above 100 K. The measuring field was 3000 Oe.

Simulations were performed with the *EasySpin* function `curry`. The g-values were taken from the EPR measurements and held constant, while the exchange coupling constant J was varied. A variable offset was taken into account in the fitting to account for the temperature-independent diamagnetism of the sample and the sample holder.

S.5 Detailed description of the simulation algorithm

Here, we discuss the algorithm to simulate EDNMR spectra of general systems in more detail, including implementation-specific aspects and the use of *EasySpin*[5] functions.

1. Generate $\hat{H}(\phi,\theta)$ for a particular orientation. Conveniently, the *EasySpin* function `sham()` has several outputs: one field-independent and three field-dependent terms, corresponding to

$$\hat{G}_{x_i} = \frac{\partial \hat{H}}{\partial B_{x_i}} \quad \text{with} \quad x_i = x, y, z \tag{3}$$

2. Diagonalize the Hamiltonian, such that $\hat{H}_d = U'\hat{H}U$. From this, the energy levels as well as all transition frequencies can be constructed. This is usually the most expensive step and prohibits the application to very large spin systems.

3. Calculate the transition probability matrix P between the eigenstates if a microwave field is applied orthogonally to the external field.

$$P = \frac{2}{\gamma_{\text{free}}^2}\left(|U'\hat{G}_xU|^2 + |U'\hat{G}_yU|^2\right) \tag{4}$$

   The prefactor normalizes the probabilities such that $P = 1$ for a spin-1/2 with the gyromagnetic ratio of the free electron. This is important to remember when experimental nutation frequencies of high-spin systems are used as an input for simulations, as they have to be scaled accordingly. This will become more important later when calculating the inversion efficiency of each transition. Note that the square sum over x and y components is an ad-hoc approximate average over the third Euler angle, which is justified in the case of CW or ENDOR spectra. Because of the non-linearity of echo detection, the detection probability is not strictly proportional to P in the case of EDNMR, but numerical tests showed very good agreement between the ad-hoc average and the explicit calculation of several orientations with respect to the microwave field (data not shown).

4. Calculate the detection probability (or probe weight) of each transition by $P_{\text{probe}} = P \cdot G(\Omega, \sigma_{\text{probe}})$, where $G(\Omega, \sigma_{\text{probe}})$ is a Gaussian function with standard deviation σ_{probe} which quantifies the excitation bandwidth of the detection sequence and depends on the pulse lengths and the integration window. The offset Ω refers to the difference between the frequency of the probed transition and the microwave detection frequency. This step effectively introduces orientation selection, analogous to the `orisel()` function in *EasySpin*. Note that all further steps can be omitted for transitions below a cut-off, corresponding to the weakest transition detectable at a realistic signal-to-noise ratio. This truncation leads to much improved computational efficiency.

5. Calculate the inversion efficiency (or pump weight) for each transition by treating it as an independent effective two-level system, which is permitted if the pump pulse is sufficiently narrow-banded to make it transition-selective with respect to the transitions with non-zero transition probability in any three-level subsystem. In other words, the pump pulse may affect several transitions without violating the assumption as long as these transitions do not share a level. Off-resonance effects of the pump pulse with respect to the pumped transitions are neglected, as they mainly introduce a power and T_2 broadening, which can be introduced ad-hoc later in a computationally much cheaper way. The problem of on-resonance irradiation of a spin-1/2 can be solved analytically even in the presence of T_2 relaxation, and from the z-value of the magnetization after the pulse, the inversion efficiency can be calculated. The effective nutation frequency for each transition is given by $\omega_1' = \omega_1(\Omega, Q) \cdot \sqrt{P}$, where $\omega_1(\Omega, Q)$ is reduced according to the resonator profile with quality factor Q. More mathematical details of this step are given below.

6. Up to this point, we have a list of transitions with corresponding frequencies, probe weights, and pump weights. With this at hand, we can calculate the EDNMR spectrum.

    (a) For each probe transition, we identify all connected pump transitions. The bookkeeping is easily achieved, as every transition ($|i\rangle \rightarrow |j\rangle$) is connected to all transitions where either i or j are the same, corresponding to a row (or column) in the diagonalized Hamiltonian. Each connection can, in principle, lead to a peak.

    (b) The frequency of the EDNMR peak is given by $f_{\mathrm{pump}} - f_{\mathrm{probe}}$.

    (c) The polarization difference $\Delta p_{\mathrm{probe}}$ of the observed transition can be calculated from a starting density matrix and the inversion efficiency of the pumped transition. Providing a density matrix different from that at thermal equilibrium as an input allows using the same function for simulating experiments where a preparation period precedes ELDOR-detected hole burning. Furthermore, spin-polarized systems can be treated that way. More details of this step are given below.

    (d) The amplitude of the EDNMR peak is given by $\Delta p_{\mathrm{probe}} \cdot P_{\mathrm{probe}}$.

7. Sum up the spectra for all orientations and all requested isotopologues. This is the easiest point to introduce parallel processing.

The general bookkeeping scheme used here allows the simulation of any kind of spin system (if the computational resources are sufficient). The implementation is general with respect to the nature of the interactions and the topology of the system. It can thus be used to simulate conventional EDNMR spectra, but it is not limited to this situation. An arbitrary distinction between allowed and forbidden transitions does not exist. Nevertheless, as mentioned above, it improves computational efficiency to use a numerical cut-off to suppress transitions that are so weakly allowed that they only marginally contribute to the detection intensity.

We would like to point out several limitations of this approach. 1) Off-resonance effects of the pumped transitions are neglected. This may become important at very high resolution, *i.e.* if the phase memory time of the electron spins is very long and no strains are present. 2) All pulses are treated as selective. This condition is certainly not always met. High-turning angle pulses may, in practice, be semi-selective, *i.e.* act on several connected transitions at once. This can generate a multitude of coherences, even on the nuclear spins. Nuclear spin coherence in turn, can be converted to observable electron coherence by an echo-detection sequence or even a $\pi/2$ pulse, with no possibility to suppress this transfer by phase cycling. Furthermore, simultaneous excitation of connected transitions causes different polarization changes than independent excitation. These effects can cause deviations between experimental and simulated spectra even for correct spin Hamiltonian parameter sets. It seems, however, that the approach fits a multitude of experimental spectra quite well. 3) The detection is not modeled explicitly. This is not a very severe restriction, as this should only affect the linewidth, which is introduced ad-hoc anyway. Our approach also does not model the central hole explicitly. For this, off-resonance and relaxation effects on the observed transitions would need to be simulated explicitly, which would be very costly. We also suspect that spin diffusion and B_1 inhomogeneities have a rather large influence on the exact shape of the central hole. These effects are hard to predict in the absence of detailed information on the resonator and sample, which is usually not available. We thus do not think that the added tremendous computational cost for explicitly simulating detection would be justified. The central hole can often be fitted and removed very well, escpecially at higher fields.

S.5.1 Calculation of inversion efficiency and polarization difference

The Bloch equations in the rotating frame, including on-resonance irradiation with ω_1, the transition probability P and transverse relaxation with time constant T_2 but neglecting longitudinal relaxation with time constant T_1, read

$$\frac{d}{dt}\vec{M}(t) = \begin{pmatrix} -\frac{1}{T_2} & 0 & 0 \\ 0 & -\frac{1}{T_2} & -\omega_1\sqrt{P} \\ 0 & \omega_1\sqrt{P} & 0 \end{pmatrix} \cdot \vec{M}(t) = \mathbf{T}\cdot\vec{M}(t) \tag{5}$$

with the solution (starting along $+z$)

$$\vec{M}(t) = \exp\left(\mathbf{T}\cdot t\right)\cdot \begin{pmatrix} 0 \\ 0 \\ 1 \end{pmatrix} \tag{6}$$

The z-component of the effective magnetization vector is then given by

$$M_z(t) = e^{-\frac{t}{2T_2}}\left(\frac{\sinh\left(\frac{bt}{2T_2}\right)}{b} + \cosh\left(\frac{bt}{2T_2}\right)\right) \tag{7}$$

with

$$b = \sqrt{1-4PT_2^2\omega_1^2} \tag{8}$$

In fact, Cox *et al.*[6] used this solution in their recently published code without giving details in the paper. From the value $M_{z,ij}$ of a given transition ($|i\rangle \rightarrow |j\rangle$), the inversion efficiency (or pump weight) W_{ij} can be calculated by

$$W_{ij} = \frac{1-M_{z,ij}}{2} \quad , \tag{9}$$

which is zero if the transition is unaffected, 1/2 for saturation and 1 for inversion. The populations p of the levels $|i\rangle$ and $|j\rangle$ *after* the hole-burning pulse are given by

$$p_i = (1-W_{ij})\cdot p_{0,i} + W_{ij}\cdot p_{0,j} \tag{10}$$

$$p_j = (1-W_{ij})\cdot p_{0,j} + W_{ij}\cdot p_{0,i} \quad , \tag{11}$$

Where p_0 denotes the population *before* the hole burning pulse. The contribution of an observed transition ($|k\rangle \rightarrow |l\rangle$) to the EDNMR signal intensity is then proportional to the polarization *difference* Δp_{kl} before and after the pulse:

$$\Delta p_{kl} = (p_l - p_k) - (p_{0,l} - p_{0,k}) \tag{12}$$

This way, we are not concerned with the exact topology of the system. Obviously, $\Delta p_{kl} = 0$ if all indices are different from each other, and we do not have to do the calculation for these pairs of transitions at all. But in the case where the pumped and the observed transition share a level, it does matter how they are connected and how the populations are distributed. In this formalism, the bookkeeping automatically retrieves this information.

The above algorithm is implemented in a MATLAB function `horseradish`, that works similar to existing *EasySpin* functions, *i.e.* one has to define a spin system, give experimental parameters, and decide on simulation options (*e.g.* cut-offs). The code was implemented in *EasySpin* version `6.0.0-dev.2`, but older versions should work just as well. One only needs to take care that the definitions of the electron-electron couplings slightly changed with respect to previous versions.

S.6 Relaxation / ESEEM data

Transverse relaxation / 2-pulse ESEEM traces obtained at X- and Q-band frequencies are shown in Fig. S8. Clearly, they are very different. At Q-band frequencies, **CuP2** does not show any nuclear modulations at all, while ***f*-CuP2** does. In X-band, **CuP2** shows oscillations corresponding to once and twice the proton Zeeman frequency, while ***f*-CuP2** shows a signal that can almost be described as 'beatings'. A detailed discussion of these remarkable differences is beyond the scope of this work, but since we observed the effect of strong level mixing in the EDNMR spectra of ***f*-CuP2**, it is not too surprising that strong ESEEM modulations are observed. It remains to be seen whether one can explain these oscillations in more detail. We can speculate that the porphyrin nitrogen atoms and the $M_S = 0$ sub-level, where the hyperfine coupling vanishes, are involved. The observed frequencies would then correspond to the nuclear Zeeman and nuclear quadrupole frequencies. The raw data are available online.

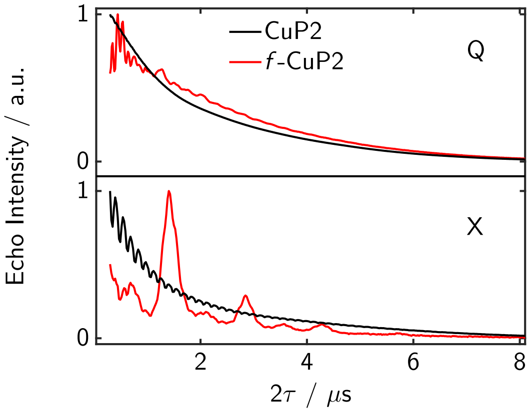

Fig. S8 Two-pulse ESEEM traces for **CuP2** and ***f*-CuP2**, recorded at X- and Q-band frequencies. All traces were acquired at the maximum of the corresponding EDFS spectrum.

S.7 Additional data for CuP2

S.7.1 Energy level diagram and EDNMR

If we consider a single copper site where all tensors are collinear and oriented along z, the first-order energy expression is

$$E(m_S, m_I) = m_S \nu_S - m_I \nu_I + m_S m_I A_{\|} + \frac{3}{2} P_{\|} m_I^2 \tag{13}$$

If we now assume that $|A_{\|}| >> |\nu_I|, |P_{\|}|$, then the ordering of the energy levels is dominated by the electron Zeeman and the hyperfine terms only. The energy level scheme is shown in Fig. S9.

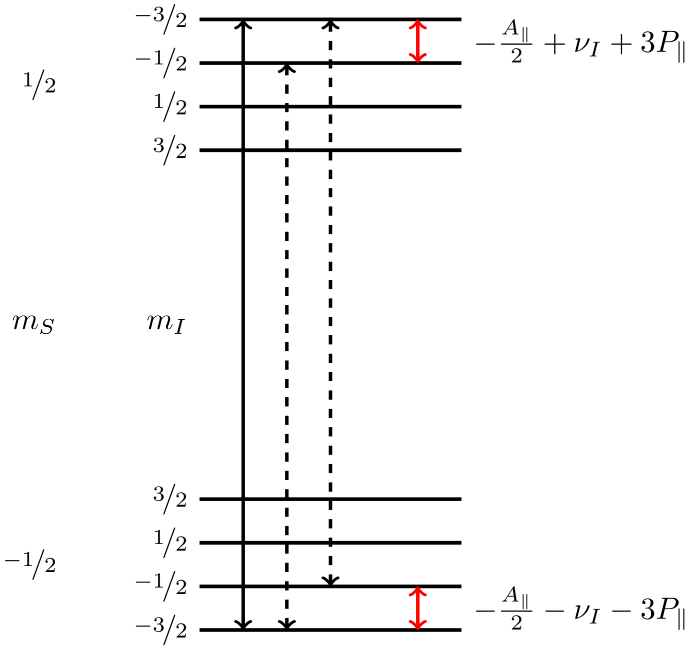

Fig. S9 Energy level scheme for a Cu(II) compound with $S = 1/2$, $I = 3/2$ with $|A_{\|}| >> |\nu_I|, |P_{\|}|$ and $A_{\|} < 0$. Black solid: Observed transition if the low-field/high-frequency edge of the spectrum is observed. Black dashed: Connected (singly) forbidden transitions that give rise to the EDNMR peaks. Red: Nuclear frequencies obtained by taking the difference between observer and hole burning frequency.

The black solid line indicates the observed transition if we set the magnetic field to the low-field/high-frequency edge of the spectrum. The connected forbidden transitions are shown as black dashed lines. It is clear that the hole burning pulse has to be applied at lower frequencies (which is the case in the experiments we show for **CuP2**). The red lines show the nuclear frequencies that are obtained by plotting the hole spectrum against $\nu_{\mathrm{Obs}} - \nu_{\mathrm{HTA}}$. While the exact frequencies and assignments of the transitions depend on the conventions and sign of the parameters, in this case the two nuclear frequencies are centered at $-|A_{\|}|/2$ and the splitting between the two side holes is given by $\Delta\nu = 2\nu_I + 6P_{\|} = 2\nu_I + e^2qQ/h$. Fortunately, *EasySpin* has transparent and consistent sign conventions.

S.8 Additional data for *f*-CuP2

S.8.1 Half-field transition

The half-field region of ***f*-CuP2** is shown in Fig. S10. The signal-to-noise ratio obtained at a concentration of about 1 mM was not sufficient to interpret the half-field spectrum confidently in terms of distance and tensor orientations.

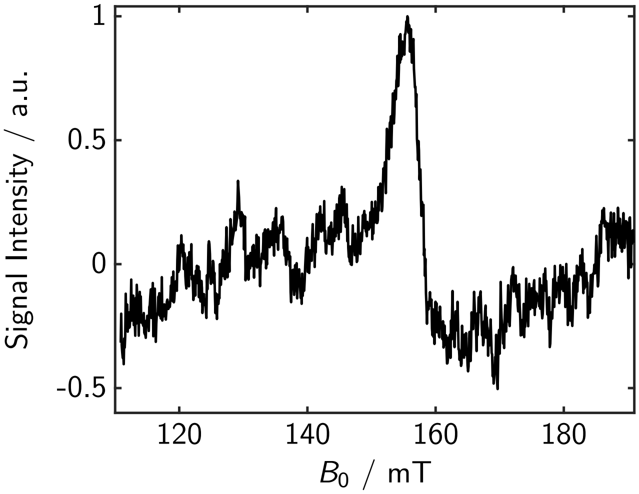

Fig. S10 Half-field region of ***f*-CuP2**.The spectrum was recorded at 20 K and a concentration of about 1 mM.

S.8.2 Resolution of ELDOR spectra

ELDOR spectra obtained at the low-field edge of the EPR spectrum of ***f*-CuP2** are shown in Fig. S11. Here, the pulses were much softer than in the main manuscript. The HTA pulse was comparable to that employed for **CuP2**. Nevertheless, the resolution is still very low. This shows that the many closely spaced side holes, intrinsic to the system, lead to the low resolution, not the strong pulses.

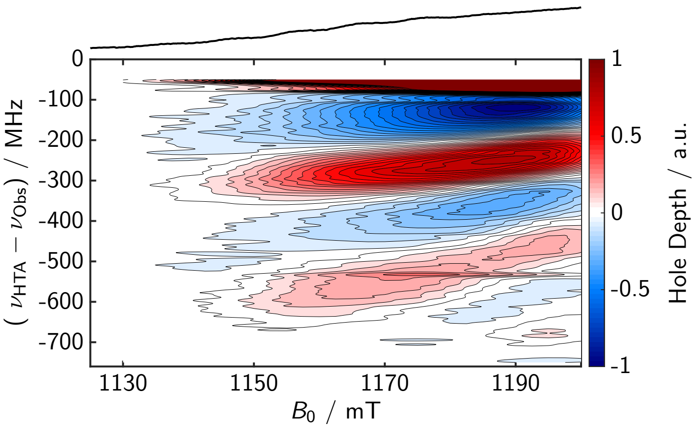

Fig. S11 ELDOR spectra recorded at the low-field edge of ***f*-CuP2**, with long, soft pulses: $t_{\mathrm{HTA}} = 20\,\mu$s and $\nu_1 \approx 1$ MHz (Resonator center). The resolution is much worse than in the case of **CuP2**, even though the experimental parameters, especially ν_1, are similar.

S.9 Nutation Experiments

In principle, nutation experiments should give information about the spin state of a species. However, in the present case, this turned out to be a challenge. The nutation curves for **CuP2** and ***f*-CuP2** are shown in Fig. S12. First, even in the case of **CuP2**, the oscillations are damped strongly. This is due to the 3 mm Q-band resonator, in which the driving field is rather inhomogeneous. In the case of ***f*-CuP2**, nearly no oscillation can be seen. This finding is the same in two different spectrometers and resonators (other data not shown).

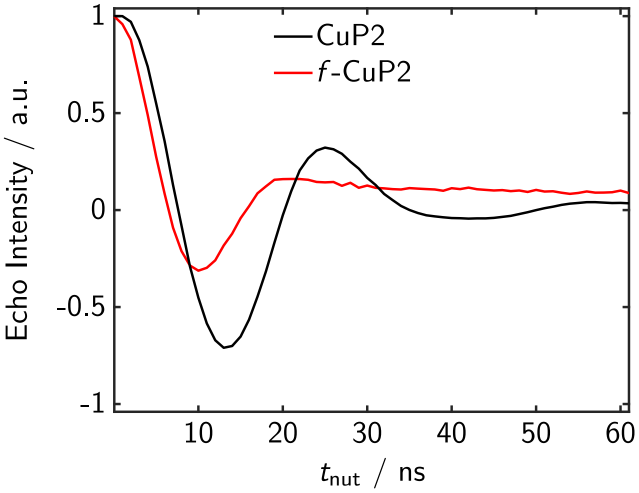

Fig. S12 Nutation curves of **CuP2** and ***f*-CuP2** recorded at the maximum of the field sweep, in the center of the resonator and at maximum power. The minimum of the nutation curve (the "π-pulse time") is about 13.5 ns in the case of **CuP2** and about 10 ns in the case of ***f*-CuP2**.

A closer analysis of the spin system revealed that a distribution of transition moments is expected in the case of ***f*-CuP2**. Fig. S13 shows the distribution of transition moments of all transitions in the spin system (excluding strictly forbidden transitions) for a particular, non-canonical orientation. The transition moments are normalized with respect to the g-factor of the free electron. In the case of **CuP2**, there are some transitions with a (relative) transition moment of about 1. The value is slightly higher because the g-factor is slightly larger than that of a free electron. These transitions are the allowed transitions. Additionally, there are some transitions with very low transition moments. These are the forbidden transitions that can be driven to yield side holes in EDNMR spectra. In the case of ***f*-CuP2**, there is a very broad distribution of transition moments. However, some of the transition moments are clearly larger than in the case of **CuP2**. This is consistent with the position of the first minimum in the nutation traces. This minimum appears around 10 ns for ***f*-CuP2**, while it appears at around 13 ns for **CuP2**. Interestingly, it is the hyperfine coupling in the $S = 1$ case that leads to the broad distribution of transition moments and not the ZFS. This can be seen in the third and fourth panel of Fig. S13.

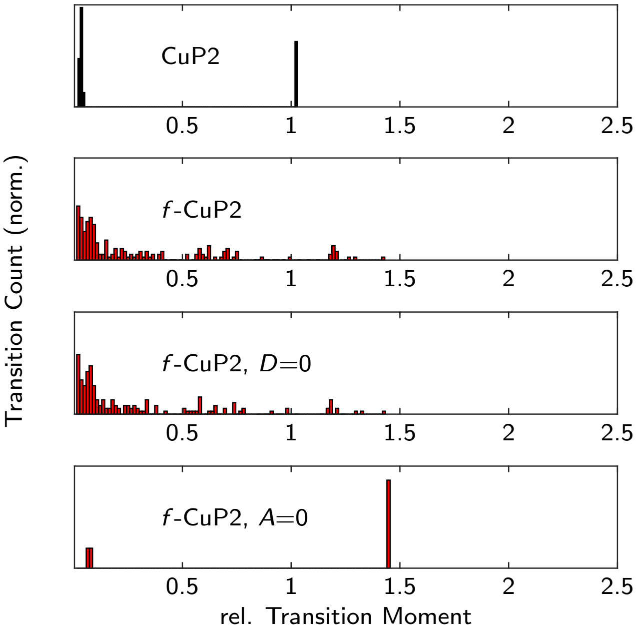

Fig. S13 Histogram of transition moments, normalized by the dimension of the respective Hilbert space. The transition moments are normalized with respect to the g-factor of the free electron. In the case of **CuP2**, there are some clearly allowed transitions with well-defined transition moments. In the case of ***f*-CuP2**, there is a broad distribution of transition moments, which, in turn, lead to damped nutation oscillations. This distribution persists if the ZFS is set to zero, but the it becomes well-defined again if the hyperfine coupling vanishes.

S.10 Concentration dependence

All the EPR measurements in the main text are conducted at a concentration of 1 mM. Since electron-electron interactions are a central part of the discussion, we verified that our results are not a result of the rather high concentration and possible aggregation. We thus measured transverse relaxation curves and representative ELDOR spectra of **CuP2** and ***f*-CuP2** at a concentration of 1 mM and also at 0.2 mM. The results are shown in Fig. S14. In conclusion, we found no significant difference between the measurements at different concentrations. Measuring at 1 mM is then highly advantageous in terms of signal-to-noise ratio and measurement time.

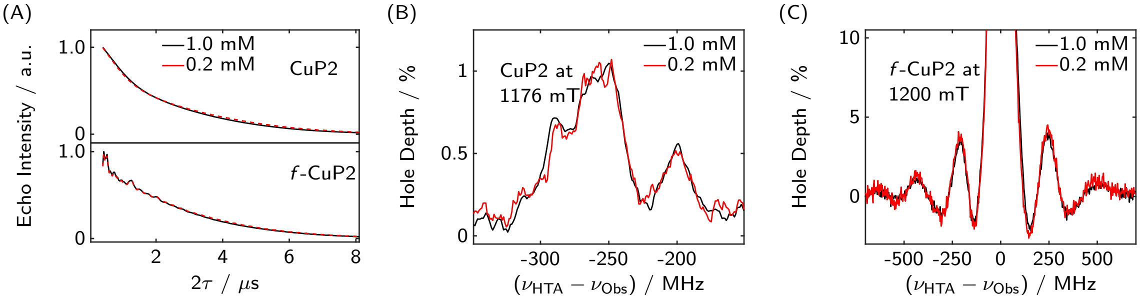

Fig. S14 Verification of the results at lower concentration. (A) Q-band 2-pulse echo decay for **CuP2** (top) and ***f*-CuP2** (bottom) at a concentration of 1 mM (black) and 0.2 mM (red). The relaxation curves are almost the same. There is a very small component that relaxes slightly faster in the more concentrated samples, but the ELDOR spectra were all recorded with τ values where this deviation is negligible. (B) Representative EDNMR spectrum of **CuP2** recorded at a concentration of 1 mM (black) and 0.2 mM (red). The latter trace was averaged for a much longer time to achieve at least a similar signal-to-noise ratio. Note that a larger step size was chosen than in Fig. 7 in the main text. While the low concentration really is a limiting factor in this measurement, the result at 0.2 mM verifies that our measurements and conclusions at 1 mM are not a result of the high concentration. (C) Representative ELDOR spectrum of ***f*-CuP2** recorded at a concentration of 1 mM (black) and 0.2 mM (red). No significant deviation is found between the two spectra, which confirms that the holes and anti-holes we observe in the case of ***f*-CuP2** are not a result of the rather high concentration.

S.11 Illustration of anti-hole correlation patterns

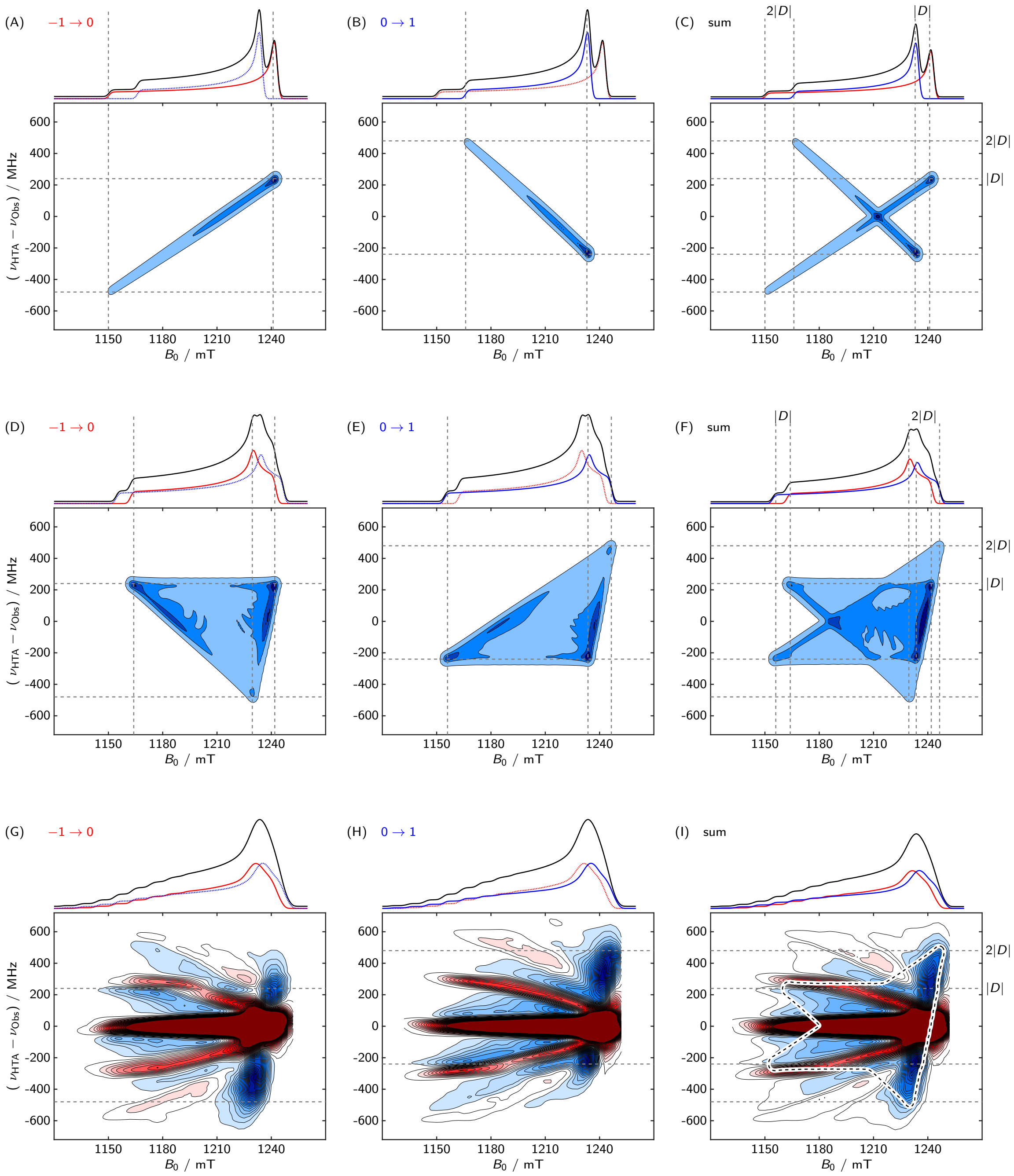

Fig. S15 Illustration of correlation patterns of the anti-holes for a spin-1 system with anisotropic $\mathbf{g}$-tensor. On top of each figure is the EPR spectrum (black) and the contributions from the $m_S \to m'_S = -1 \to 0$ (red) and $0 \to 1$ (blue) transitions. Note that a change of sign of D would interchange the labelling of the transitions. The first two plots of each row show the hypothetical, field-correlated ELDOR spectra in the case where only one of the two EPR manifolds would be observed, while the third one shows the sum. A ZFS with $|D| = 240$ MHz was used for all simulations. (A)-(C): No hyperfine interaction. $\mathbf{D}$- and $\mathbf{g}$-tensor axial and collinear. (D)-(F): No hyperfine interaction. $\mathbf{D}$- and $\mathbf{g}$-tensor twisted by 90 degrees. (E)-(F): Spin system with parameters of ***f*-CuP2**. In (I), the correlation pattern of (G) was overlaid. In the high-field region, where the ZFS splitting is much larger than the hyperfine splitting, the anti-hole correlation patterns overlay quite well. In the low-field region, the hyperfine interaction considerably interferes with the ZFS because the induced splittings are close to each other.

S.12 Simulated single orientation spectra

The spectrum of an effective electron spin $S = 1$ coupled to two copper nuclei is of considerable complexity, even for a single orientation. This is visible in Fig. S16, where also a comparison to a single copper site with $S = 1/2$ is shown. Note that the top spectrum also includes a ZFS with a magnitude comparable to that of the hyperfine coupling.

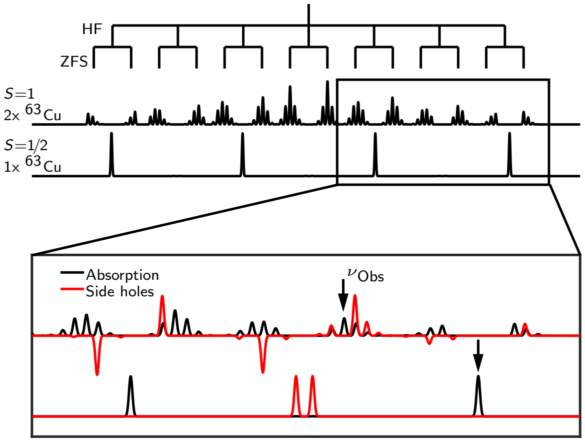

Fig. S16 Top: Absorption spectra of a single orientation of a typical Cu(II) monomer and a strongly exchange coupled dimer. The $S = 1$ system includes a ZFS with $D = -240$ MHz. Bottom: Zoom of absorption spectra as well as EDNMR spectra with the observer frequency indicated by an arrow. If the side holes have a counterpart in the absorption spectrum, the transitions are not strongly forbidden.

The orientation was chosen such that the forbidden transitions in the $S = 1/2$ case are not strictly forbidden, *i.e.* the magnetic field was not along the canonical orientation of the hyperfine tensor. The bottom of Fig. S16 shows the absorption spectra, and, overlaid, the EDNMR spectra with the observer frequency indicated by arrows. The simulation assumed a nominal flip angle of π for the HTA pulse. The EDNMR spectra were then renormalized for clarity. This means that every side hole that has a visual counterpart in the absorption spectrum is *not* strongly forbidden, and the side holes that have *no* counterpart *are* strongly forbidden. The latter case is best seen in the EDNMR spectrum of the $S = 1/2$ system. Clearly, in the $S = 1$ system, corresponding to ***f*-CuP2**, it is very hard to have an intuitive understanding of the energy level scheme and the transitions that are allowed and forbidden, and what hole pattern will emerge from that. This is where our implementation of the algorithm is very helpful, as it does not need any predefined knowledge about the spin system, and about which transitions are connected.

S.13 Intensities of forbidden transitions for $S = 1/2$ and $S = 1$

The comparison of the ELDOR spectra of **CuP2** and ***f*-CuP2** shows that the intensity of the side holes is much larger in the case of ***f*-CuP2**. The double-quantum transitions are clearly visible for ***f*-CuP2** while we could not observe them at all for **CuP2**. This is even more striking because we used a high turning angle pulse that was much shorter for ***f*-CuP2** compared to **CuP2**. A more detailed theoretical analysis revealed that this is in fact an intrinsic property of a $S = 1$ spin system that is strongly coupled to a nucleus.

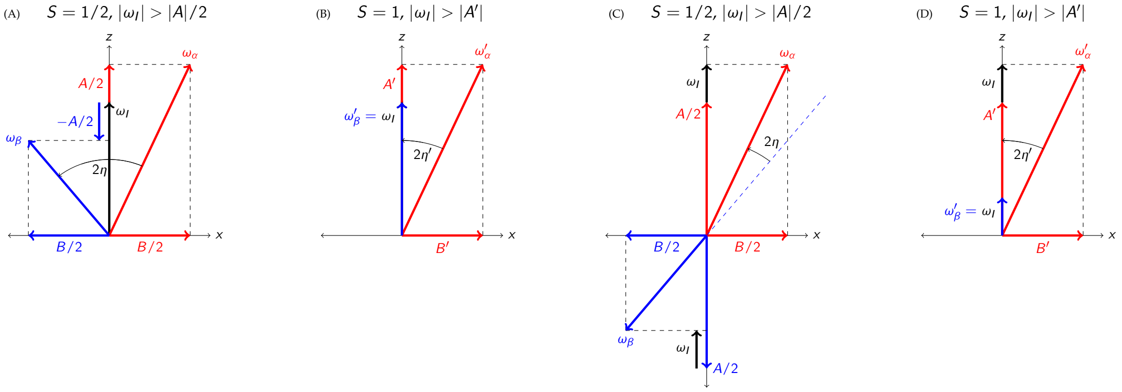

(A) $S = 1/2$, $|\omega_I| > |A|/2$

(B) $S = 1$, $|\omega_I| > |A'|$

(C) $S = 1/2$, $|\omega_I| > |A|/2$

(D) $S = 1$, $|\omega_I| > |A'|$

Fig. S17 Schematic illustration of the effective fields (quantization axes) at a nucleus with $I = 1/2$ coupled to an electron spin with $S = 1/2$ or $S = 1$ in the weak and strong coupling regimes. In the case of $S = 1$, the α and β substates belong to a fictitious spin-1/2. In the particular case of (B) and (D), the β substate corresponds to $M_S = 0$, where the hyperfine components vanish. Note that for very strong couplings, *i.e.* $|A| >> \omega_I$, the two quantization axes in the different electron spin manifolds are exactly antiparallel for $S = 1/2$ and the intensities of forbidden transitions vanish. For $S = 1$, this is not the case, because the hyperfine field vanishes in the $M_S = 0$ subspace.

Fig. S17 shows the quantization axes/effective fields for a nucleus with $I = 1/2$. The $S = 1/2$ case, (A) and (C), is textbook knowledge.[7] The direction of the quantization axes of the nucleus depends on the state of the electron spin. The forbidden transitions have a probability of $\mu_\mathrm{f} = \sin(\eta)$, where 2η is the angle between the different effective fields at the nucleus. Without any pseudosecular term, the axes are exactly anti-parallel and the forbidden electron-nuclear transitions are strictly forbidden. With $B \neq 0$, the forbidden transitions become partially allowed. A peculiarity of $S = 1$ systems is the vanishing hyperfine contribution in the $M_S = 0$ substate. If there is no nuclear quadrupole interaction, and if the high-field approximation is valid for the electron spin, the quantization axis in this substate is strictly along z. In the case of **CuP2** and ***f*-CuP2**, the hyperfine coupling is much larger than the nuclear Zeeman frequency for most of the orientations, *i.e.* the strong coupling case applies. For a spin-1/2, 2η tends to zero and hence the intensities of the forbidden transitions also tend towards zero for $|A| \gg |\omega_I|$, as is apparent from Fig. S17(C). Interestingly, this is not the case for $S = 1$, as can be seen in Fig. S17(D).

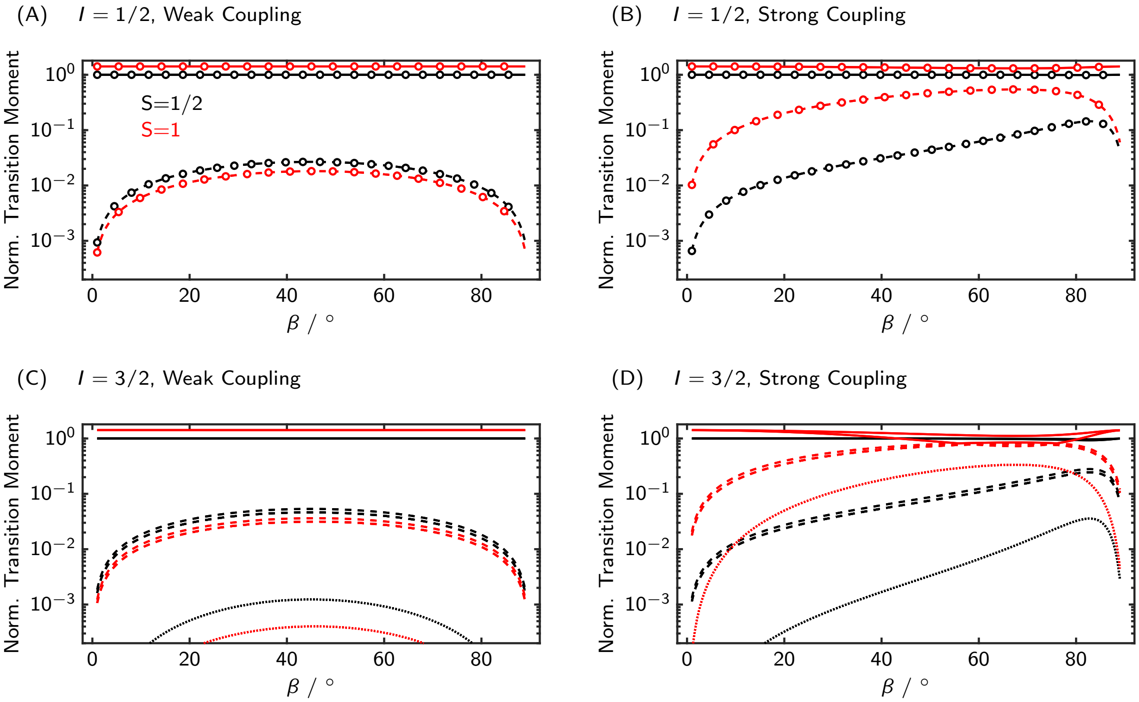

Fig. S18 Transition moments of allowed transitions (solid lines), singly forbidden transitions ($\Delta m_I = \pm 1$, dashed lines) and doubly forbidden transitions ($\Delta m_I = \pm 2$, dotted lines) of a system with $S = 1/2$ (black) or $S = 1$ (red). The angle β refers to the angle between the unique axis of the axial hyperfine tensor and the static magnetic field. In the cases with $I = 1/2$ ((A) and (B)), the analytical calculations are shown as circles. Weak coupling: ν_I=150 MHz, $A_{\parallel}$=20 MHz, $A_{\perp}$=4 MHz. Strong coupling: ν_I=13 MHz, $A_{\parallel}$=600 MHz, $A_{\perp}$=80 MHz. Note that in the $S = 1$ case, the hyperfine coupling was halved and the transition moments of the strictly allowed transitions are a factor of $\sqrt{2}$ higher. The relevant case for **CuP2** and ***f*-CuP2** is (D). It is clearly visible that the forbidden transitions are orders of magnitude larger in the $S = 1$ case, even if only one nucleus is coupled to it. For many orientations, the doubly forbidden transitions of ***f*-CuP2** are even more intense than the singly forbidden transitions of **CuP2**.

S.14 Effect of exchange coupling on ENDOR

Here we provide a more detailed discussion why the ENDOR spectra of **CuP2** and ***f*-CuP2** are expected to be the same, although the two samples correspond to the weak and strong exchange-coupling limits, respectively.

Let m_{S1} and m_{S2} be the z-projection of electron spins 1 and 2, and m_{I1} and m_{I2} the corresponding quantum numbers of nuclear spins 1 and 2. We assume that the hyperfine coupling constants A_{ij} between electron i and nucleus j are $A_{11} = A_{22} = A$ and $A_{12} = A_{21} = 0$. Further, we define $M_S = m_{S1} + m_{S2}$ and $M_I = m_{I1} + m_{I2}$.

In the strong exchange-coupling limit, the singlet and the triplet states are well separated. The $|m_{S1}m_{S2}\rangle = |\alpha\alpha\rangle$ and $|\beta\beta\rangle$ states are the same in the uncoupled and the coupled basis (labeled in the latter case as $|T_1\rangle$ and $|T_{-1}\rangle$, respectively), while the exchange coupling mixes the $|\alpha\beta\rangle$ and $|\beta\alpha\rangle$ into $1/\sqrt{2}(|\alpha\beta\rangle + |\beta\alpha\rangle) = |T_0\rangle$ and $1/\sqrt{2}(|\alpha\beta\rangle - |\beta\alpha\rangle) = |S_0\rangle$. To first order, the energy levels, excluding the exchange coupling, are given by

$$\frac{1}{h}E\left(M_S, m_{I1}, m_{I2}\right) = M_S \nu_S + \left(m_{I1} + m_{I2}\right)\nu_I + M_S\left(m_{I1} + m_{I2}\right)A' \tag{14}$$

Where $A' = A/2$ is half the coupling in the uncoupled case.[8] The EPR transition frequencies ($\Delta M_S = 1$, $\Delta M_I = 0$) in the absence of ZFS are then given by

$$\frac{1}{h}\Delta E\left(M_S \to M_S + 1, M_I\right) = \nu_S + M_I A' \tag{15}$$

As expected, the splitting between the EPR transitions, corresponding to unit difference in M_I, is halved compared to the uncoupled case. On the other hand, the ENDOR (or NMR, $\Delta M_S = 0$, $\Delta M_I = 1$) transitions are given by

$$\frac{1}{h}|\Delta E\left(M_S, M_I \to M_I + 1\right)| = |M_S \cdot A' + \nu_I| \qquad . \tag{16}$$

The absolute value is given because ENDOR experiments can usually not distinguish between positive and negative frequencies, except when circularly polarized radiofrequency irradition is used.[9] The apparent hyperfine coupling is still $A' = A/2$, but the contribution of the coupling to the ENDOR transitions is scaled by $M_S = \pm 1$ and is thus doubled compared to the uncoupled case, where $m_S = \pm 1/2$.

In summary, while the effective hyperfine coupling is halved in the coupled case, the M_S values are doubled, and the nuclear frequencies thus stay the same in the M_S manifolds where they are observable. In the $M_S = 0$ manifold, there is effectively no hyperfine coupling. The transitions appear at the Zeeman frequency of the nuclei (if we neglect the nuclear quadrupole), but the ENDOR effect is expected to be much smaller because of the missing hyperfine enhancement.

S.15 Additional data for figures

Here we give detailed information on each figure. This includes information about raw data and processing scripts which are deposited on an institutional repository with a permanent doi: (`https://doi.org/10.3929/ethz-b-000323948`). The files are in a mixed format. Data recorded on Bruker spectrometers are in ASCII-format and readable by any text editor. Since our home-built spectrometer is run *via* MATLAB© (The MathWorks, Inc), even the raw data are stored in `.mat` files. Since *EasySpin* is *the* standard simulation library (written in MATLAB) in the EPR community, we believe that a majority of readers will be able to read and run the scripts we provide. Note that the `.mat` files can also be read into the free software R, with the help of the library 'R.matlab' (https://cran.r-project.org/web/packages/R.matlab/). Nevertheless, there are many processing steps between the raw data and the actual spectra, since our spectrometer saves echo transients that oscillate at an intermediate frequency. In order to allow a quick investigation of the spectra, we also converted the most important experimental spectra to plain ASCII-files. Note, however, that they cannot be regarded as true raw data files.

Fig. 5 (A)

X-Band CW spectrum of **CuP2**. 1 mM in toluene. 40 μl of the solution in a 3 mm outer diameter tube. Recorded on a Bruker Elexsys E500 spectrometer with an SHQ resonator and a liquid helium flow cryostat. Temperature: 20 K, Field modulation: 100 kHz with 5 G amplitude (some features were better resolved with a smaller modulation amplitude, but this led to much worse SNR. This is the reason why the background was acquired with a smaller modulation amplitude than the spectrum, but scaled accordingly), time constant: 81 ms, conversion time 327 ms,$\nu_{\mathrm{mw}} = 9.402271$ GHz, microwave power: 0.4004 mW (27 dB). The spectrum was background-corrected with the spectrum of pure toluene. The simulation was scaled to the experimental spectrum by lsq-fitting including a constant offset correction. The magnetic field was calibrated with an external DPPH standard.

Raw data and processing scripts:
Matlab processing and simulation:
`Cu_SL_Xcw.m` and `Cu_SL_Sys.m`
raw file spectrum:
`CuSL_cw_20K_Rg50_27dB_5Gmod_tc81_tconv327`
raw file background:
`bg_20K_0p5mod_50RG_27dB_24scans`

Fig. 5 (B)

Q-band echo detected field sweep of **CuP2**. Same sample as in (A). Recorded on the home-built AWG based spectrometer with the 3 mm resonator with large bandwidth. Temperature: 15 K, $\nu_{\mathrm{mw}} = 35.5$ GHz, pulse sequence $t_p/2 - \tau - t_p - \tau - echo$, $t_p = 200$ ns, $\tau = 500$ ns, integration window 256 ns (same echo parameters as for the EDNMR measurements, see below). Shot repetition time 4 ms. +/- phase cycle of the first pulse and the detection, 50 shots each, 1 average. 512 magnetic field points. The simulation was scaled to the experimental spectrum by lsq-fitting including a constant offset correction.

Raw data and processing scripts:
Matlab processing and simulation:
`Cu_SL_Qedfs.m` and `Cu_SL_Sys.m`
raw file spectrum:
`20180802_1153_fieldswp.m`
processed experimental x/y data as ASCII file:
`Cu_SL_Qedfs.txt`

Fig. 6 (A)

Q-band EDNMR spectra of **CuP2** at the low-field edge of the EDFS spectrum (field given in the figure). All parameters the same as in Fig. 5 (B) unless stated otherwise. Pulse sequence $t_{\mathrm{HTA}} - T - t_p/2 - \tau - t_p - \tau - echo$. t_{HTA}= 20 μs (Gaussian), $\nu_1 \approx 5$ MHz (resonator center), $T = 1\,\mu$s. +/- phase cycle of the HTA pulse, combined with a +/- phase cycle of the $\pi/2$ pulse. The echo detection was the same as for the EDFS, but the integration window was 500 ns. ν_{HTA} swept from -400 to -150 MHz relative to ν_{Obs}, in steps of 0.5 MHz (500 steps), random acquisition mode. 1 shot per point, 20 x 100 averages. At each field a reference echo intensity was acquired of which the EDNMR echo intensity was subtracted. This way, lower echo intensities (holes) correspond to positive EDNMR peaks. A Gaussian smoothing was applied to the experimental spectra. For each magnetic field, the simulated spectrum was adjusted to the experimental one by fitting the overall intensity, the linewidth, and a first order baseline (the latter step effectively accounts for the central hole, which is approximately linear at large offsets).

Raw data and processing scripts:

Matlab processing and simulation:

`Cu_SL_EDNMR_zz_zoom` and `Cu_SL_Sys.m`

raw file 2D spectrum:

`./Cu_SL_ednmr_B_field_correlation_zz_zoom/ Cu_SL_zz_zoom_EDNMR.mat`

This data is already patched together from many individual files per field position. The patching is done with the script '`raw_data_to_matlab_struct.m`'.

The (real) raw data files are in `./Cu_SL_ednmr_B_field_correlation_zz_zoom/data/`

processed experimental x/y data as ASCII file:

`Cu_SL_EDNMR_zz_zoom.txt`

Fig. 6 (B)

Q-band EDNMR spectra of **CuP2** over the whole range of the EDFS spectrum (field given in the figure). All parameters are the same as in Fig. 6 (A) unless stated otherwise. t_{HTA}= 10 μs (Gaussian), $\nu_1 \approx 2$ MHz (resonator center). ν_{HTA} swept from -700 to 700 MHz relative to ν_{Obs}, in steps of 1.4 MHz (1000 steps), random acquisition mode. 1 shot per point, 3 x 50 averages. For each magnetic field position, a region around the central hole and the proton signals were omitted. The rest of the spectrum was then normalized. Subsequently, the simulated spectrum was fitted to the experimental ones as explained above.

Raw data and processing scripts:

Matlab processing and simulation:

`Cu_SL_EDNMR_overview` and `Cu_SL_Sys.m`

raw file 2D spectrum:

`./Cu_SL_ednmr_B_field_correlation_overview/ Cu_SL_overview_EDNMR.mat`

This data is already patched together from many individual files per field position. The patching is done with the script '`raw_data_to_matlab_struct.m`'.

The (real) raw data files are in `./Cu_SL_ednmr_B_field_correlation_overview/ data/`

processed experimental x/y data as ASCII file:

`Cu_SL_EDNMR_overview.txt`

Fig. 7 (A)

Q-band EDNMR spectrum of **CuP2** at 1176 mT and simulation indicating the orientation selection. All parameters are the same as in Fig. 6 (B) unless stated otherwise. ν_{HTA} swept from -450 to -100 MHz relative to ν_{Obs}, in steps of 0.35 MHz (1000 steps), random acquisition mode. 1 shot per point, 500 averages.

Raw data and processing scripts:

Matlab processing and simulation:

`Cu_SL_orisel.m` and `Cu_SL_Sys.m`
raw file spectrum:
`20180803_1059_fstep_EDNMR.mat`
processed experimental x/y data as ASCII file:
`Cu_SL_EDNMR_1D_goodSNR.txt`

Fig. 7 (B)

Q-band EDNMR spectrum of **CuP2** at 1176 mT and simulations with different orientations and electronic couplings. All parameters are the same as in Fig. 7 (A).

Raw data and processing scripts:
Matlab processing and simulation:
`Cu_SL_EDNMR_1D_goodSNR` and `Cu_SL_Sys.m`
raw file spectrum:
`20180803_1059_fstep_EDNMR.mat`
processed experimental x/y data as ASCII file:
`Cu_SL_EDNMR_1D_goodSNR.txt`

Fig. 8 (A)

X-Band CW spectrum of ***f*-CuP2**. 1 mM in toluene. 40 μl of the solution in a 3 mm outer diameter tube. The experimental details are the same as in Fig. 5 (A) if not stated otherwise. $\nu_{\mathrm{mw}} = 9.402493$ GHz. Field modulation: 100 kHz with 2 G amplitude, time constant: 81 ms, conversion time 327 ms, microwave power: 0.2007 mW (30 dB). The spectrum was background-corrected with the spectrum of pure toluene (with slightly different power settings, which were compensated for by a relative scaling). The simulation was scaled to the experimental spectrum by lsq-fitting including a constant offset correction.

Raw data and processing scripts:
Matlab processing and simulation:
`Cu_fused_Xcw.m` and `Cu_fused_Sys.m`
raw file spectrum:
`Cu_fused_cw3_20K_2mod_RG50_30dB`
raw file background:
`bg_20K_0p5mod_50RG_27dB_24scans`

Fig. 8 (B)

Q-band echo detected field sweep of ***f*-CuP2**. Same sample as in (A). Recorded on the home-built AWG based spectrometer with the 3 mm resonator with large bandwidth. Temperature: 15 K, $\nu_{\mathrm{mw}} = 35.5$ GHz, pulse sequence $t_p/2 - \tau - t_p - \tau - echo$, $t_p = 32$ ns, $\tau = 400$ ns, integration window 256 ns (same echo parameters as for the EDNMR measurements, see below). Shot repetition time 2 ms. +/- phase cycle of the first pulse and the detection, 500 shots each, 1 average. 1024 magnetic field points. The simulation was scaled to the experimental spectrum by lsq-fitting including a constant offset correction.

Raw data and processing scripts:
Matlab processing and simulation:
`Cu_fused_Qedfs.m` and `Cu_fused_Sys.m`
raw file spectrum:
`20181206_1401_fieldswp.m`
processed experimental x/y data as ASCII file:
`Cu_fused_Qedfs.txt`

Fig. 9 (A-F)

Field-correlated ELDOR spectra of ***f*-CuP2**. All parameters the same as in Fig. 8 (B) unless stated otherwise. Pulse sequence $t_{\mathrm{HTA}} - T - t_p/2 - \tau - t_p - \tau - echo$. t_{HTA}= 50 ns (Gaussian), $\nu_1 \approx 40$ MHz (resonator center), $T = 1$ μs, $\tau = 500$ ns. +/- phase cycle of the HTA pulse, combined with a +/- phase cycle of the $\pi/2$ pulse. Integration window 500 ns. ν_{HTA} swept from -700 to 700 MHz relative to ν_{Obs}, in steps of 2.8 MHz (500 steps), random acquisition mode. The magnetic field was stepped from 1140 to 1248 mT in steps of 3 mT. Shot repetition time 4 ms. 10 shots per point, 2 x 6 averages. At each field a reference echo intensity was acquired of which the EDNMR echo intensity was subtracted. This way, lower echo intensities (holes) correspond to positive EDNMR peaks. A Gaussian smoothing was applied to the experimental spectra.

Raw data and processing scripts:
Matlab processing and plotting:
(A,B) `Cu_fused_EDNMR_overview.m`
(C,D) `Cu_fused_EDNMR_add_J.m`
(A,B) `Cu_fused_EDNMR_add_D.m`
Experimental Data:
`./Cu_fused_ednmr_B_field_correlation/ Cu_fused_EDNMR.mat`
This data is already patched together from many individual files per field position. The patching is done with the script '`raw_data_to_matlab_struct.m`'.
The (real) raw data files are in `./Cu_fused_ednmr_B_field_correlation/data/`
processed experimental x/y data as ASCII file:
`Cu_fused_EDNMR_overview.txt`
Simulated Data:
`Cu_fused_ednmr_simulations/` (The names of the files are self-explanatory)
Simulation Script:
`Cu_fused_ednmr_simulations/`
`List_of_systems.m` and `EDNMR_2D_simulation.m`

Fig. 10 (A) and (B)

(A) Same data as in in Fig. 6 (B), but plotted as a filled contour plot. (B) Same data as in in Fig. 9 (A).

Raw data and processing scripts:
Matlab processing and plotting:
`Cu_fused_vs_Cu_SL_EDNMR.m`

Fig. 11

Magnetic susceptibility measurements of ***f*-CuP2** and the corresponding monomer **CuP$_{\mathbf{H}}$**. The measurement field was 3000 Oe, and no background correction was performed.

Raw data and processing scripts:
Matlab processing and plotting:
`SQUID.m`
raw files:
`BL_monomer_MvT_full_3000Oe.dc.TXT`
`BL_dimer_MvT_full_3000Oe.TXT`

Fig. 12

Q-band ($\approx$34 GHz) ENDOR spectra of **CuP2** and ***f*-CuP2**. Pulse sequence $t_p - T - t_p/2 - \tau - t_p/2 - \tau - echo$ with t_p= 40 ns, an evolution period $T = 27$ μs during which a 25 μs RF π was applied. The inter-pulse delay τ was chose to be 220 ns. The whole echo signal was integrated and recorded as a function of the RF frequency in stochastic mode with an RF increment of 0.1 MHz. The RF power was adjusted based on a nutation experiment.

Raw data and processing scripts:

Matlab processing:
`Cu_SL_fused_QENDOR`
raw files:
CuP2
(x,y): `19_Davies_P2Cu2_tol_15K_11955G_n5000`
(z): `20_Davies_P2Cu2_tol_15K_11130G_n5000`
***f*-CuP2**
(x,y): `08a_Davies_f-P2Cu2_tol_15K_11790G_n5000`
(z): `10_Davies_f-P2Cu2_tol_15K_11125G_n9200`

Fig. S8

Q-band and X-band ESEEM traces of **CuP2** and ***f*-CuP2**. Pulse sequence $t_p/2 - \tau - t_p - \tau - echo$ with t_p= 32 ns, recorded at the maximum of the respective EDFS spectra. The value of τ was increased from 150 ns in steps of 12 ns (400 steps in total). A a +/- phase cycle of the $\pi/2$ pulse was used.

Raw data and processing scripts:

Matlab processing:
`ESEEMS.m`
raw files:
CuP2
(Q): `20181208_1102_2pecho_ESEEM`
(X): `20181205_1329_2pecho_ESEEM.m`
***f*-CuP2**
(Q): `20181206_1623_2pESEEM_12350G_avg1`
(X): `20181205_1036_2pESEEM_3290G_avg1`
processed experimental x/y data as ASCII file:
CuP2
(Q): `Cu_SL_Q_ESEEM.txt`
(X): `Cu_SL_X_ESEEM.txt`
***f*-CuP2**
(Q): `Cu_fused_Q_ESEEM.txt`
(X): `Cu_fused_X_ESEEM.txt`

References

1 F. C. Grozema, C. Houarner-Rassin, P. Prins, L. D. A. Siebbeles and H. L. Anderson, *Journal of the American Chemical Society*, 2007, **129**, 13370–13371.

2 S. Richert, B. Limburg, H. L. Anderson and C. R. Timmel, *Journal of the American Chemical Society*, 2017, **139**, 12003–12008.

3 A. Doll and G. Jeschke, *Journal of Magnetic Resonance*, 2017, **280**, 46–62.

4 A. Doll, S. Pribitzer, R. Tschaggelar and G. Jeschke, *Journal of Magnetic Resonance*, 2013, **230**, 27 – 39.

5 S. Stoll and A. Schweiger, *Journal of Magnetic Resonance*, 2006, **178**, 42–55.

6 N. Cox, A. Nalepa, W. Lubitz and A. Savitsky, *Journal of Magnetic Resonance*, 2017, **280**, 63–78.

7 A. Schweiger and G. Jeschke, *Principles of Pulse Electron Paramagnetic Resonance*, Oxford University Press, 2001.

8 E. J. L. McInnes and D. Collison, *eMagRes*, 2016, **5**, 1445–1458.

9 A. Schweiger and H. H. Günthard, *Molecular Physics*, 1981, **42**, 283–295.